Available online at www.sciencedirect.com

ScienceDirect

Advances in Space Research 72 (2023) 1052–1069

ADVANCES IN SPACE RESEARCH (a COSPAR publication)

www.elsevier.com/locate/asr

Automatic built-up area extraction by feature-level fusion of Luojia 1–01 nighttime light and Sentinel satellite imageries in Google Earth Engine

Farhad Samadzadegan [a], Ahmad Toosi [a], Farzaneh Dadrass Javan [a,b,*]

[a] School of Surveying and Geospatial Engineering, University College of Engineering, University of Tehran, Tehran, Iran
[b] Faculty of Geo-Information Science and Earth Observation (ITC), University of Twente, Enschede, the Netherlands

Received 22 November 2022; received in revised form 14 February 2023; accepted 9 May 2023
Available online 23 May 2023

Abstract

Today, with the non-stop expansion of urbanization, mapping urban areas and monitoring their dynamic changes have become challenges for governments and also a hot topic for researchers. Remote sensing imageries play a key role in urban studies, the extraction of urban built-up areas, and monitoring their changes. A variety of studies have proposed methods for the extraction of regional, national, and global built-up areas. However, the majority of them used limited features and applied a manual sample selection strategy for classification, leading to time-consuming and low-efficient algorithms. This paper proposes a fully automatic procedure to real-time extract built-up areas by integrating the Luojia 1–01 nighttime lights (NTL) images, Sentinel-2 multispectral data, Sentinel-1 Radar images, and SRTM elevation data in cloud-computing Google Earth Engine. Firstly, potential built-up areas (PBA) and non-built-up areas (NBA) are obtained by applying Otsu and multi-level thresholding to some of the extracted spectral-textural-spatial (STS) features and by applying logical rules. Secondly, built-up and non-built-up samples are automatically selected and are used to train a Support Vector Machine (SVM) supervised classifier and to classify the hybrid feature set so that a preliminary classified map (PCM) can be obtained. Thirdly, the PCMs are automatically corrected using the non-built-up area, and morphological operations in the so-called post-classification to provide a refined classified map (RCM) and final built-up map. Four study areas in Northern America, Europe (Scandinavia), the Middle East, and Eastern Asia were selected to test the proposed method. Also, five state-of-the-art built-up products, accompanied by Google Earth images, were used as the reference data. The results indicate that the proposed method can accurately and automatically select samples and map built-up areas with a spatial resolution of 10 m. Its performance is validated with an average overall accuracy of 94.4% and an average Kappa coefficient of 0.89 and by visual comparison of our method results with other reference data. The proposed method has significant potential to be used in real-time extracting built-up areas and in monitoring their dynamic changes on national and global scales.

Keywords: Built-up mapping; Nighttime light; Luojia 1–01; Cloud computing; Big data

1. Introduction

Urban built-up areas, as living spaces for the majority of humans and a place for their activities, have rapidly expanded in recent decades (Jafari and Attarchi, 2021; Liu et al., 2019). Due to the fast rate of urbanization expansion, it is one of the most challenging issues for governments and policy-makers (Esch et al., 2017). With this regard, the accurate mapping of built-up areas and monitoring their dynamic changes is crucial for decision makers to manage better human lives (Liu et al., 2019). Compared

* Corresponding author.
E-mail address: f.dadrassjavan@utwente.nl (F. Dadrass Javan).

https://doi.org/10.1016/j.asr.2023.05.015
0273-1177/

to mapping built-up areas on the ground, which is so time-consuming and expensive, remote sensing (RS) science and technology provide experts with the opportunity to accurately extract built-up areas and monitor their dynamic changes (Liu et al., 2019; Zhou et al., 2017). Therefore, accurate and fast extraction of urban built-up areas has always been a hot topic for researchers in RS (Djerriri et al., 2019).

A variety of studies have been conducted so far on the topic of urban built-up mapping, which from different points of view can be categorized as follows:

(a) *Categorization based on method or technique:* In this point of view, the literature can be categorized into techniques that used spectral, spatial, or textural indices (Bhatti and Tripathi, 2014; Djerriri et al., 2019; Ghosh et al., 2018; He et al., 2010; Hidayati et al., 2018; Prasomsup et al., 2020; Risky et al., 2017; Zhang et al., 2014). With this regard, we may mention those who implemented supervised classification as an intelligent tool (Liu et al., 2019; Wang et al., 2020a, 2020b), those who applied the threshold-based built-up extraction technique (Li et al., 2018), the papers that used the deep learning (DL)-based method (Brown et al., 2022; He et al., 2019; Huang et al., 2018; Tan et al., 2018; Tan et al., 2020; Tan et al., 2021; Tian et al., 2018; Li et al., 2016; Li et al., 2022; Zhang and Tang, 2018), and the articles that conducted LULC mapping based on the super-resolution technique (Chen et al., 2018a; Jia et al., 2019; Wang et al., 2018; Wang et al., 2020a, 2020b).

(b) *Categorization based on data:* Some studies benefited from the radar images as a feature of built-up extraction (Ban et al., 2015; Dell'Acqua and Gamba, 2006; Esch et al., 2017; Farhadi et al., 2022; Holobâcă et al., 2019; Jafari and Attarchi, 2021; Lino et al., 2018; Mohammadnejad, 2020; Semenzato et al., 2020; Zhou et al., 2017). High-resolution satellite imageries were the input data for different studies which focused on built-up mapping in regional scales (Chen et al., 2018b; Iannelli et al., 2014; Huang et al., 2018; Tao et al., 2013; Li et al., 2015; Tian et al., 2018; Weizman and Goldberger, 2009; Zhang et al., 2017). A group of researchers used moderate/low-resolution data such as MODIS, Landsat, or Sentinel-2 images for their works (Gong et al., 2013; Bhatti and Tripathi, 2014; Darmanto et al., 2015; Ettehadi et al., 2019; Guo et al., 2018; Lefebvre et al., 2016; Rasul et al., 2018; Prasomsup et al., 2020; Wang et al., 2017; Weizman and Goldberger, 2009; Zhang and Tang, 2018; Zhang and Wang, 2014). The nighttime light (NTL) satellite images also were one of the most fashionable data that are regularly used for built-up mapping purposes. In this case, scholars primarily used the Defense Meteorological Satellite Program (DMSP) and Operational Linescan System (OLS) images for this task (Cao et al., 2009; Hu et al., 2017; Li et al., 2017; Li and Zhou, 2017; Lu et al., 2008; Small et al., 2005; Xie and Weng, 2016; Yan, 2019; Yu et al., 2014; Zhang et al., 2013; Zhou et al., 2014). Afterwards, by launching the Visible Infrared Imaging Radiometer Suite Day/Night Band carried by the Suomi National Polar-orbiting Partnership (NPP-VIIRS) satellite with relatively better spatial resolution, compared with the DMSP-OLS data, it was majorly used for urban monitoring and built-up extraction (Chen et al., 2020; Dou et al., 2017; He et al., 2014; Li et al., 2018; Liu et al., 2019; Small et al., 2013; Xie et al., 2014; Xu et al., 2016; Xu et al., 2020; Yang et al., 2019; Yu et al., 2018; Yuan et al., 2019; Zou et al., 2017). Nowadays, the Chinese Luojia (LJ) 1–01 satellite NTL images with the highest available spatial resolution (130 m) are used for built-up mapping (He et al., 2021; Li et al., 2018; Wang et al., 2021).

(c) *Categorization based on the extent of the study area:* From this standpoint, the literature can be classified into three groups: those who worked on a regional scale (Lu et al., 2008; Wang et al., 2017a), those who focused on a national scale (Ghorbanian et al., 2020), and the works that provided outputs for the whole globe (Ban et al., 2015; Esch et al., 2017; Sharma et al., 2016).

The expansion of urban environments is taking place rapidly, and to monitor and manage these urban areas, many up-to-date and accurate maps are required. Since the methods mentioned above do not allow the user to effectively produce up-to-date maps for any parts of the Earth in a short time we developed a fully automatic framework that uses open-access RS data, real-time cloud-based image processing tools, and efficient artificial intelligence (AI) algorithms to produce urban built-up maps for any given study area and any time. For this purpose, inspired by Liu et al. (2019) and in continuation of our previous research on automatic LULC mapping (Toosi et al., 2022), in this paper, an improved, automatic, and real-time built-up area extraction method was proposed, which integrates LJ 1–01 NTL data, Sentinel-1 and Sentinel-2 imageries, and SRTM DEM. In the developed method, first, a hybrid feature space is established. Second, a variety of built-up and non-built-up training and validation samples are collected automatically using multi-level/Otsu thresholding and logical rules. Third, the training samples are used for machine learning (ML)-based supervised classification to obtain a preliminary classified map. Then, it is corrected within a two-level post-classification phase to obtain a fine classified thematic map and built-up map. By using numerous powerful features, the fully automatic proposed algorithm can reduce the confusion between built-up areas and other similar land coverages,

thereby improving the accuracy of built-up area mapping.

The main contribution of this paper is to establish a fast and simple method that enables the users to automatically extract built-up areas at no charge for any desired region of interest at any time using well-established powerful ML techniques and open-access satellite data.

2. Materials and methods

2.1. Study area

The following four areas from North America, Europe (Scandinavia), the Middle East, and Eastern Asia were selected as study areas: Mexico City, Mexico; Stockholm, Sweden; Tehran, Iran; and Seoul, South Korea (Fig. 1). The above-mentioned study areas which are chosen randomly are from continents with different climates, urban structures, and levels of economic condition. The choice of these four areas allows us to validate the proposed method with different built-up area distribution characteristics and to show the ability of the method for the efficient and automatic extraction of urban built-up areas.

2.2. Dataset

We used 10 m Sentinel-2 level-2A multispectral imageries, 10 m Sentinel-1 SAR images, and 130 m LJ 1–01 NTL data from the year 2018 for the selected study areas as input data. The dataset is described in Table 1 and is shown in Fig. 2. We used cloud-free Sentinel-2 images for a short period of time within a year to avoid any issues caused by any noticeable changes to built-up areas over time. Sentinel-2 images are bottom of atmosphere (BOA) or surface reflectance (SR) products which are not affected by the atmosphere. The preprocessed Sentinel-1, Sentinel-2, and SRTM DEM data were called back from the Google Earth Engine (GEE) dataset repository (https://developers.google.com/earth-engine/datasets/), while the LJ 1–01 images were downloaded from the official website of Hubei data and application network (https://www.hbeos.org.cn; https://59.175.109.173:8888/).

2.3. Processing tool

The GEE cloud computing platform is used to access a variety of open-source geospatial data without the need to download them. On the other hand, some levels of preprocessing (i.e. geometric and atmospheric corrections) were applied by the developers to the data which can facilitate working with big satellite data.

3. Methodology

According to the block diagram in Fig. 3, the proposed method of this study is made up of three steps including "data preparation and feature extraction," "classification and post-classification," and "validation" which are separately described as follows:

3.1. Data preparation and feature extraction

In this initial step, the Sentinel-1 SAR images are called back from the GEE data repository, filtered by the boundary (for each study area) and date (for the year 2018), and all the available polarization/bands (in these case studies VV and VH are available) are selected. Then, the subtraction of VV and VH (VV-VH) and their average ($\frac{VV+VH}{2}$) are calculated as features since they can help to discriminate built-up areas from other land coverages (Lino et al.,

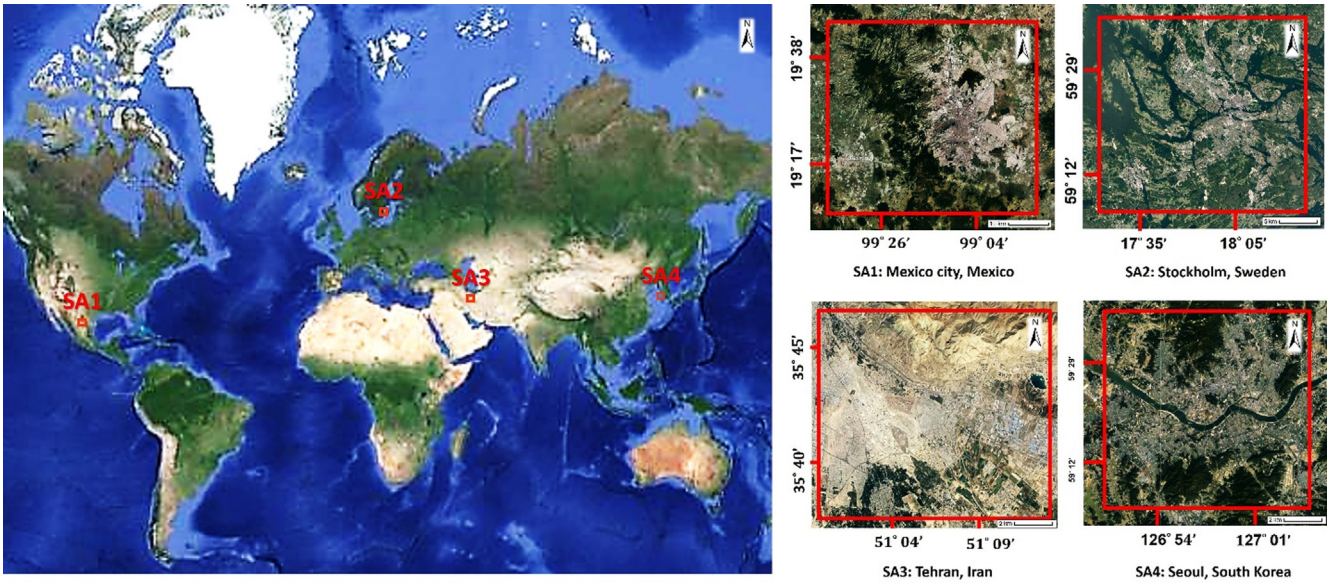

Fig. 1. Location of the study areas.

Table 1
Data descriptions.

Satellite	Bands (Polarization)	Resolution (m)	Total No. of Images
Sentinel-1	C (VV and VH)	10	287
Sentinel-2	RGB, RedEdge, NIR, and SWIR	10–60	73
SRTM	Elevation	90	4
LJ 1–01	–	130	4

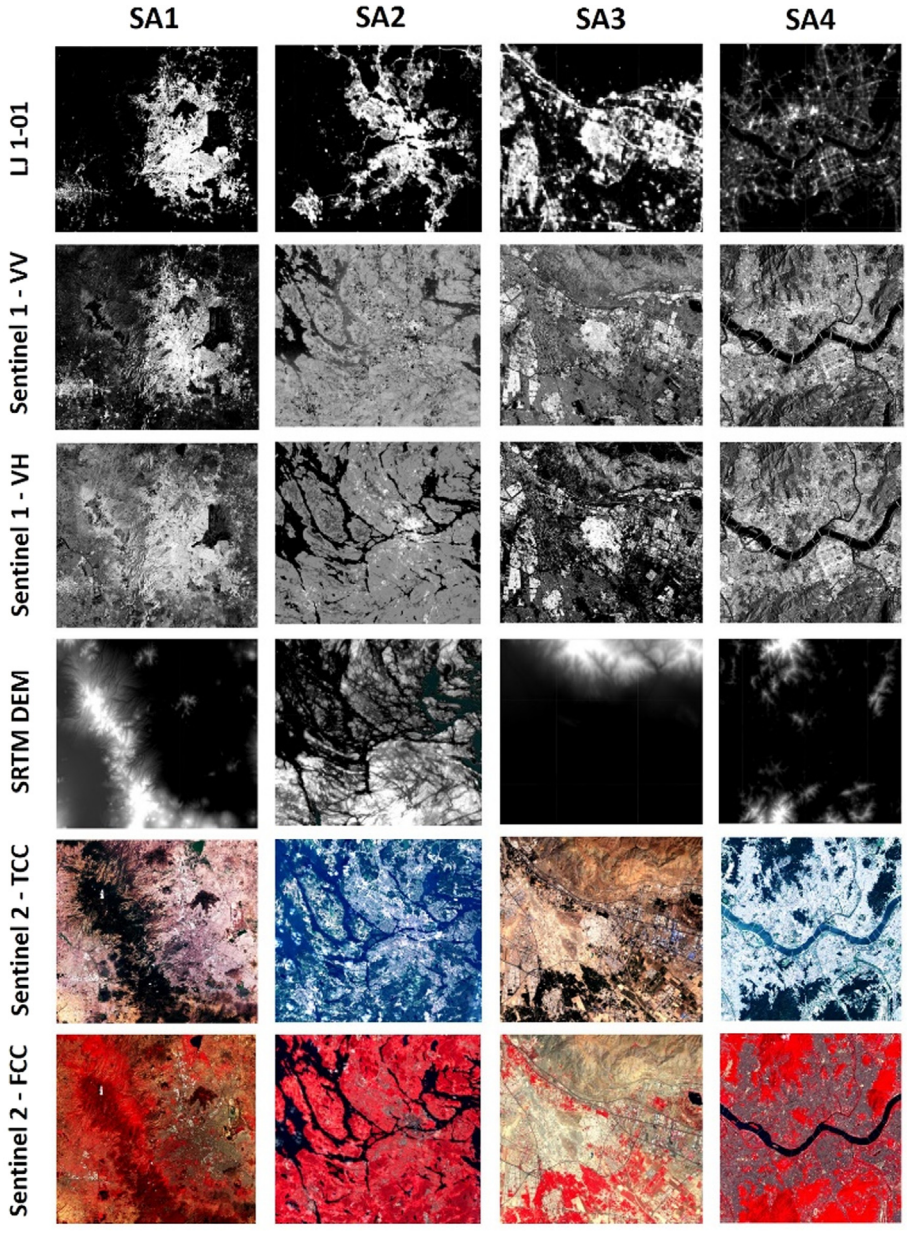

Fig. 2. Presentation of the dataset.

2018). For Sentinel-2 data, the images are called back in GEE and filtered by the boundary of study areas. Then, the remaining images are filtered by date (the summer season was set for the date duration to have the least cloudy or foggy pixels) and "percentage of cloudy pixels" where only the images with cloudy pixels less than 1% are selected. All the spectral bands having a spatial resolution of more than 10 m are manipulated (resampled) so that all the channels can reach a spatial resolution of 10 m (since the Sentinel-2 dataset lacks a high-resolution panchromatic band that has complete spectral coverage with other bands, no pansharpening operation has been carried out). Since built-up areas

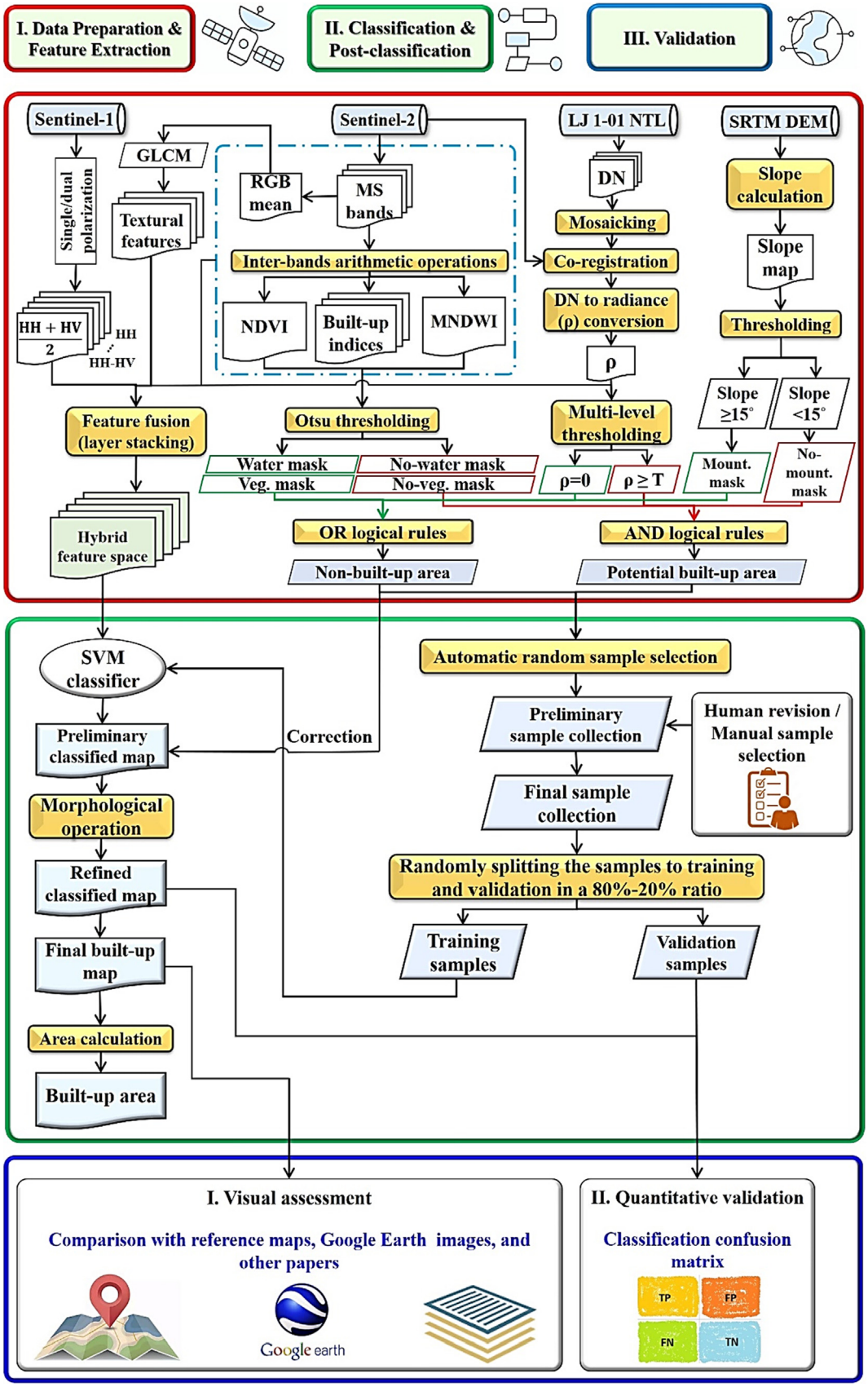

Fig. 3. Flowchart of the proposed built-up extraction method.

have different textures compared to other land coverages, the first group of features that are obtained from the average of three original 10 m-visible (RGB) bands of the Sentinel-2 dataset is textural indices which are used for discriminating built-up from non-built-up areas. We calculated 11 commonly used textural descriptors including mean, variance, homogeneity, contrast, dissimilarity, second moment, correlation, prominence, inertia, shade, and entropy which are calculated from Gray-Level Co-occurrence Matrices (GLCM) (Haralick et al., 1973). The formulas related to the textural indices are provided in Table 2.

The second group of features is seven built-up indices including Normalized Difference Built-up Index (NDBI) (Zha et al., 2003), Built-up Index (BUI) (He et al., 2010), Built-up Area Extraction Index (BAEI) (Bouzekri et al., 2015), New Built-up Index (NBI) (Jieli et al., 2010), Vegetation Index Built-up Index (VIBI) (Stathakis et al., 2012), Index-based Built-up Index (IBI) (Xu et al., 2008), and Urban Index (UI) (Kawamura, 1996). A brief description of the above-mentioned indices, accompanied by other spectral indices including Normalized Difference Vegetation Index (NDVI), Modified Normalised Difference Water Index (MNDWI) (McFeeters, 1996), and Soil Adjusted Vegetation Index (SAVI) (Huete, 1988), is provided in Table 3.

The SRTM slope maps and the features derived from the arithmetic combination of Sentinel-1 Radar bands form the spatial feature set. Due to their relatively coarse spatial resolution, the SRTM slope maps are not included in the hybrid feature set (which will be imported into the classification), and they are only used for masking mountainous areas. It is noteworthy that as the radar backscatterings are sensitive to the spatial pattern of the phenomenon, we categorized them as spatial features, and as their main duty, they can help to identify built-up areas (Semenzato et al., 2020). Furthermore, as their secondary task, radars can effectively help us in discriminating water and vegetation from other objects (Bioresita et al., 2018).

Table 2
Textural features.

Index	Formula
Mean	$\mu_x/\mu_y = \sum_{i=0}^{G}\sum_{j=0}^{G} P(i,j) \times i/j$ (1)
Variance	$\sigma_i^2/\sigma_j^2 = \sum_{i=0}^{G-1}\sum_{j=0}^{G-1} P(i,j) \times (i/j - \mu_i)^2$ (2)
Homogeneity	$\sum_{i=0}^{G-1}\sum_{j=0}^{G-1} \frac{P(i,j)}{1+\lvert i-j\rvert}$ (3)
Contrast	$\sum_{i=0}^{G}\sum_{j=0}^{G} P(i,j) \times (i-j)^2$ (4)
Dissimilarity	$\sum_{i=0}^{G-1}\sum_{j=0}^{G-1} P(i,j) \times \lvert i-j\rvert^2$ (5)
Second Momentum	$\sum_{i=0}^{G-1}\sum_{j=0}^{G-1} (P(i,j))^2$ (6)
Correlation	$\sum_{i=0}^{G-1}\sum_{j=0}^{G-1} \frac{(i,j)\times P(i,j) - (\mu_x \times \mu_y)}{\sigma_x \times \sigma_y}$ (7)
Prominence	$\sum_{i=0}^{G-1}\sum_{j=0}^{G-1} (i+j-2\sigma)^4 \times P(i,j)$ (8)
Inertia	$\sum_{i=0}^{G}\sum_{j=0}^{G} (i-j)^2 \times P(i,j)$ (9)
Shade	$\sum_{i=0}^{G-1}\sum_{j=0}^{G-1} (i+j-2\sigma)^3 \times P(i,j)$ (10)
Entropy	$-\sum_{i=0}^{G-1}\sum_{j=0}^{G-1} P(i,j) \times \log(P(i,j))$ (11)

* *P(i,j):* the relative frequency with which two pixels occur within a given neighborhood; *i* and *j*: pixels' intensity values; *G:* number of grey levels.

The Otsu thresholding is used to provide a threshold to obtain water, no-water, vegetation, and no-vegetation masks. It segments the indices by exhaustively searching for the optimum threshold (T) that minimizes the intra-class variance (Eq. (22)).

$$\delta_w^2(t) = w_1 \times \delta_1^2(T) + w_2 \times \delta_2^2(T) \tag{22}$$

where $\delta_1^2(T)$ and $\delta_2^2(T)$ are variances of the two desired classes and $w_1 = \sum_{i=0}^{T-1} p(i)$ and $w_2 = \sum_{i=0}^{L-1} p(i)$ are the probabilities of the two classes separated by T (Sezgin et al., 2004; Toosi et al., 2022).

As the LJ 1–01 NTL images are not covered by the GEE data repository, it is necessary to freely download them from the official website of the Hubei data and application network and then upload them to the GEE platform. Regarding the breadth of products, image mosaicking is necessary for case studies extending more than 250 km × 250 km. For some case studies, there may be slight spatial misregistration between the LJ 1–01 and Sentinel data that in such cases LJ 1–01 should be co-registered to Sentinel-2 10 m bands, for instance. The basic format of data is the digital numbers (DN) which are converted to radiance (ρ) according to the exponential relation of Eq. (23).

$$\rho = DN^{3/2} \times 10^{-10} \tag{23}$$

where ρ is the input radiance ($W/(m^2 sr \mu m)$) and DN is an abbreviation for the digital number of the LJ 1–01 images.

Afterward, multilevel thresholding is applied to ρ in order to obtain ρ = 0 (completely dark areas on the Earth) and ρ ≥ T (T is a threshold that presents highly lit-up areas on the Earth[1]). The reason is that the NTL images are correlated with human activities and that built-up areas have higher DN values, compared to natural non-built-up areas with very low DN values (and sometimes the values are equal to zero) (Liu et al., 2019). It is noteworthy that the LJ data are not significantly affected by different types of noises (Li et al., 2019).

SRTM Digital Elevation Data (DEM) Version-4 is called back in GEE, and its elevation band is filtered by boundary and date. Then, the slope map is calculated from the DEM layer. T = 15° is used as a threshold to obtain mountain and no-mountain masks. T = 15° is the most common threshold, which is used in studies conducted for built-up mapping (Ban et al., 2015). The AND and OR logical rules are applied to all the masks obtained from the SRTM, LJ 1–01 and Sentinel-2 data to make two base regions called potential built-up area (PBA) and non-built-up area (NBA). The AND operator states that PBA is an

[1] Regarding the minimum and maximum DN values, the threshold T is a number that segments the top n% of DNs (n can be any number, i.e., 10, 20, etc.) from the total DN values.

Table 3
Spectral features.

Index	Formula
NDVI	$(NIR - Red)/(NIR + Red)$ (12)
MNDWI	$(Green - SWIR1)/(Green + SWIR1)$ (13)
SAVI	$((NIR - Red)/(NIR + Red + 0.5)) \times 1.5$ (14)
NDBI	$(SWIR1 - NIR)/(SWIR1 + NIR)$ (15)
BUI	$NDBI - NDVI$ (16)
BAEI	$(Red + L)/(Green + SWIR); L = 0.3$ (17)
NBI	$(SWIR \times Red)/NIR$ (18)
VIBI	$NDVI/(NDVI + NDBI)$ (19)
IBI	$(NDBI - (SAVI + MNDWI)/2)/(NDBI + (SAVI + MNDWI)/2$ (20)
UI	$(((SWIR - NIR)/(SWIR + NIR)) + 1.0) \times 100$ (21)

area that has high light-up and at the same time is neither covered by vegetation nor located on steep slopes. In addition, the OR operator indicates that NBA is the summation of completely dark (with no nighttime light) areas or areas with steep slopes or covered with water/vegetation (at least one of the conditions is needed so that it can true). On the other hand, all the spectral, textural, and spatial features are stacked together to obtain a hybrid feature space.

3.2. Classification and Post-classification

A variety of sample points are randomly and automatically selected in the PBA and NBA regions. The samples are generated based on the GEE "RandomPoints" function which generates points that are uniformly random on the sphere and are within the given region (GEE Ref., 2022). For random sample generation, the given polygon, which are our study area, is decomposed into n different triangles ($i = \{1, 2, 3, \cdots, n\}$) with vertices V_{1i}, V_{2i}, and V_{3i}. Therefore, a random point (P_j) can be generated uniformly within triangle $V_{1i}V_{2i}V_{3i}$ according to the convex combination of the vertices (Eq. (24)).

$$P_j = (1 - \sqrt{w_{1i}}) \times V_{1i} + (\sqrt{w_{1i}} \times (1 - w_{2i})) \times V_{2i} + (\sqrt{w_{1i}} \times w_{2i}) \times V_{3i} \quad (24)$$

where w_{1i} and w_{2i}, which are called convex weights, are uniformly and randomly drawn from the range of [0,1] for the ith triangle. It is also noteworthy that always $\sum(w_1, w_2) = 1$ (GIS, 2011; Osada et al., 2002; SOF, 2011).

A preliminary sample collection is obtained, which can also be improved by human supervision/revision. It is noteworthy that a manual sample selection module is also set up, which allows the human expert to manually add some samples or delete some of them. After the final sample collection is prepared, it is then split into training and validation samples in an 80%-20% ratio. The training samples are used to train the Support Vector Machine (SVM) as one of the most fashionable ML supervised classification methods (Yang et al., 2018), and the validation samples are used to evaluate the classification performance. It is worth noting that here, traditional ML methods are used instead of DL-based methods so that they can be suitable for real-time, fast (as one of the goals of our proposed method), and precise processing. This is because despite the relatively higher accuracy of DL methods (Karaca et al., 2017), training of DL models is so time-consuming in comparison to traditional methods and the time will increase drastically with the increase in the size of study areas (Yilmaz et al., 2020). It is also noteworthy that in many cases, the well-established traditional ML methods, such as SVM, can provide comparable results to the DL methods (Lai, 2019). The classification process provides a preliminary classified map (PCM). Post-classification operations are set up to improve PCM. Post-classification is conducted in two steps including (1) overlaying NBA to the PCM, and then (2) applying morphological operations, i.e. opening and closing. In the first step, the NBA is overlaid to the PCM (Eq. (25)), i.e. an AND logical operation is performed between the PCM and NBA binary images. Assume the pixels in the PCM that are related to built-up and non-built-up classes be shown by 1 and 0, respectively. Also, the pixels with 1 in the NBA indicate the pixels that are definitely non-built-up. Thus, the refined classified map (RCM) obtained by overlaying (RCM_{OL}) is a binary image in which the misclassified pixels are corrected.

$$RCM_{OL} = PCM \,|\, \{(PCM = 1) \,\&\, (NBA \neq 1)\} \quad (25)$$

where | denotes conditional equality, which means that RCM is the same as PCM with the condition that the statement in the braces is exerted on the PCM. In the second level, RCM_{OL} is refined by morphological opening and closing (Eq. (26)) to remove small misclassified pixels (speckles) and to close (fill) the gaps and holes in the classified map.

$$RCM_F = (RCM_{OL} \circ H) \cdot H = (((RCM \ominus H) \oplus H) \oplus H) \ominus H \quad (26)$$

where RCM_F is the final version of RCM. The opening, closing, erosion, and dilation are presented by "o, ȯ, ⊖, and ⊕", respectively. Also, H represents the structural element. After post-classification, the final built-up map is

obtained, and the area of built-up area can be calculated using the obtained maps, if necessary.

3.3. Validation

Validation is done in both quantitative and qualitative manners. In the former method, the evaluation is conducted using the elements of confusion (error) matrix, while in the latter, the assessment is done visually by comparing the obtained results with base high-resolution Google Earth images, state-of-the-art reference maps, and the result of other studies. In our error matrix, rows and columns correspond to reference and predicted classes (BU: built-up and NBU: non-built-up), respectively. The elements of the error matrix are the User's Accuracy (UA), Producer's Accuracy (PA), Overall Accuracy (OA), and Kappa Coefficient (KC). UA indicates the probability that a classified built-up pixel is truly a built-up area. On the other hand, PA calculates the probability that a built-up pixel is correctly identified. OA indicates the proportion of pixels that are correctly identified. Finally, KC is an indicator that indicates the agreement between classified results and ground truth. UA, PA, OA, and KC are defined as Eqs. (27)–(30), respectively.

$$UA_i = \frac{X_{ii}}{X_{+i}} \times 100 \tag{27}$$

$$PA_i = \frac{X_{ii}}{X_{i+}} \times 100 \tag{28}$$

$$OA = \left(\frac{1}{N}\sum X_{ii}\right) \times 100 \tag{29}$$

$$KC = \frac{N\sum X_{ii} - \sum X_{i+}X_{+i}}{N^2 - \sum X_{i+}X_{+i}} \tag{30}$$

where X_{ii} represents the number of pixels that are correctly identified, X_{i+} is the number of pixels that belong to class i, X_{+i} is the number of pixels identified as class i, and N is the total number of image pixels (Li et al., 2018; Pearson and Blakeman, 1904).

4. Results and discussions

Fig. 4 presents the overall hybrid spectral, textural, and spatial (STS) feature space including 65 feature images in four study areas. In the case of textural descriptors, the descriptors are obtained by setting the parameters as follows (based on the GEE's default): The size of the neighborhood is set to 1, and a 3 × 3 square window is utilized, leading to four GLCMs with the offsets (−1,−1), (0,−1), (1,−1), and (−1,0). It is noteworthy that to avoid the low-quality STS features, i.e. features containing high noise or with relatively low contrast, the quality of features can be assessed both visually and numerically using the simple no-reference quality assessment metrics such as Standard Deviation, BRISQUE, DIIVINE, BLIINDS-II, SSEQ, BIQI, etc. (here we used the well-established Standard Deviation metric) (Al-Wassai and Kalyankar, 2012; Javan et al., 2019; Mhangara et al., 2020) This led to keeping only the high-quality STS features (that properly discriminate between the phenomena) and deleting useless features from the feature set.

As mentioned before, built-up indices form a significant portion of spectral index groups. According to Fig. 5, which shows the correlation between the corresponding pixels of built-up indices for SA1 (as an example), it can be seen that except in a few cases (with a weak correlation or R≈0) there is a significant positive correlation (R) between different pairs of indices at the level of $\alpha = 0.01$ in a two-tailed statistical test. What is more important than the correlation of indices is the ability of indices to discriminate between different land covers (the high power of the indices to perform such a task is indicated in Fig. 4).

Fig. 6 shows the obtained PBA and NBA accompanied by the Otsu thresholding outputs, i.e., water mask and vegetation mask. The thresholds of the histograms, i.e. T1-T8 are the Otsu thresholds that segment the water-covered and vegetated areas. The sample points including training feature collection and validation feature collection for both built-up and non-built-up classes are presented in Fig. 7. Table 4 contains information on the number of sample points. It is noteworthy that the number of samples is set by trial and error, which provides the best outcomes. Due to the computational load issue and the more accurate selection of samples and avoiding the selection of mixed pixels instead of pure pixels, a point-wise selection method was used instead of the polygon-based strategy. Hence this strategy can lead to a relatively faster classification process and more accurate and reliable results (Toosi et al., 2022). Furthermore, the manual sample selection method for large-scale case studies such as provinces, countries, and continents is so time-consuming; in some cases, human-based errors may emerge. Thus, we believe the automatic sample selection strategy of our method seems to be more efficient, which decreases the number of mistakes.

In order to tune the SVM supervised classifier parameters, the default values of GEE's references are considered, i.e. Radial Basis Function (RBF) is chosen as the kernel type, and γ and cost parameters are set to 0.5 and 10, respectively. SVM is trained by training features, and then the hybrid feature set is introduced to the classifier. By producing the initial classified maps, the produced maps are morphologically corrected using opening and closing operations with circle-shaped normalized Boolean structural elements (kernels) of radius 1 to obtain the RCMs. The mentioned 3 × 3 kernel is expressed as [0, 0.2, 0; 0.2, 0.2, 0.2; 0, 0.2, 0]. In this matrix, the semicolons separate the rows, and the colons separate the elements in each row. The RCM_F and the final built-up map for all study areas are produced, which are shown in Fig. 8.

The confusion (error) matrix for the classification performance in all study areas is presented in Fig. 9. The average overall accuracy (OA) and Kappa coefficient (K) were calculated as 94.4% and 0.89, respectively. According to the USGS standard limit (OA ≥ 85 %), all the classification

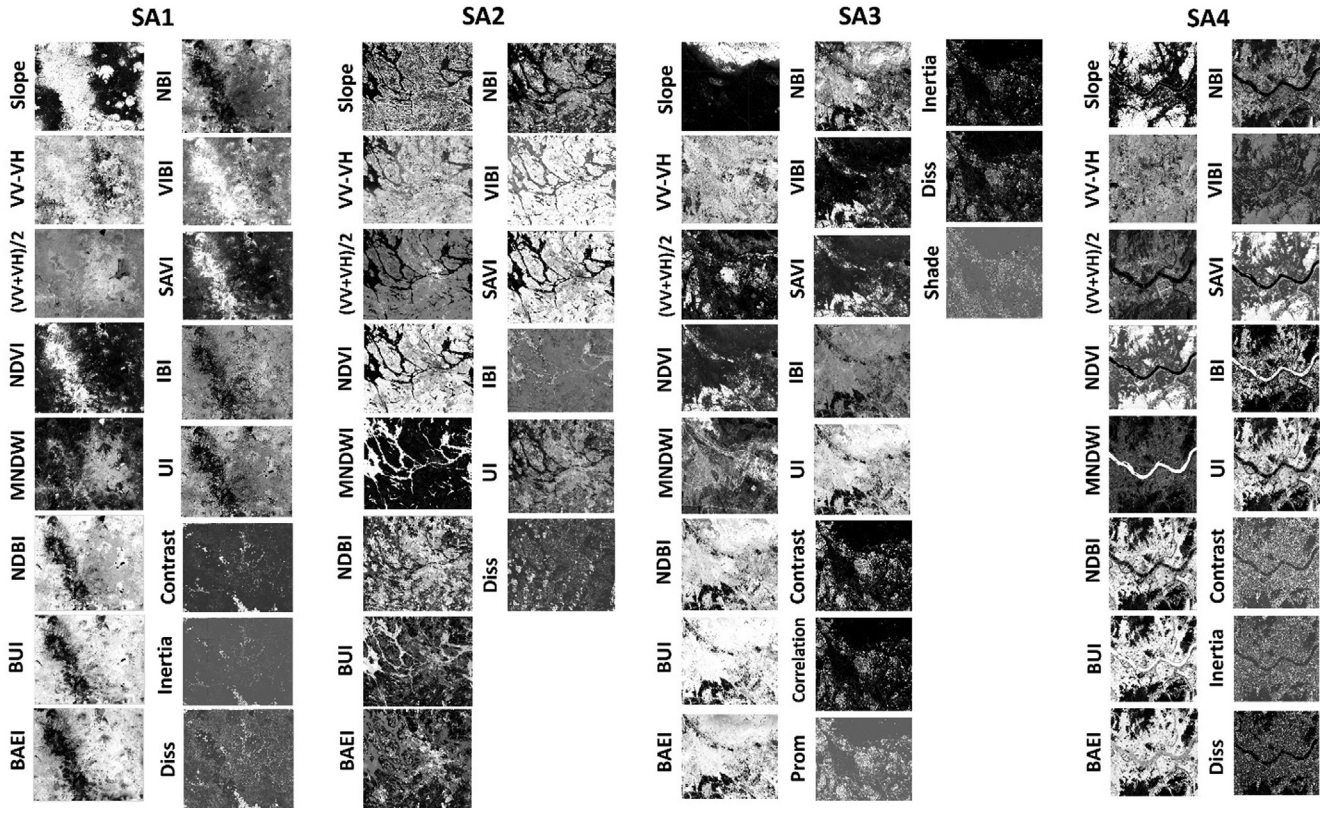

Fig. 4. The STS hybrid feature space.

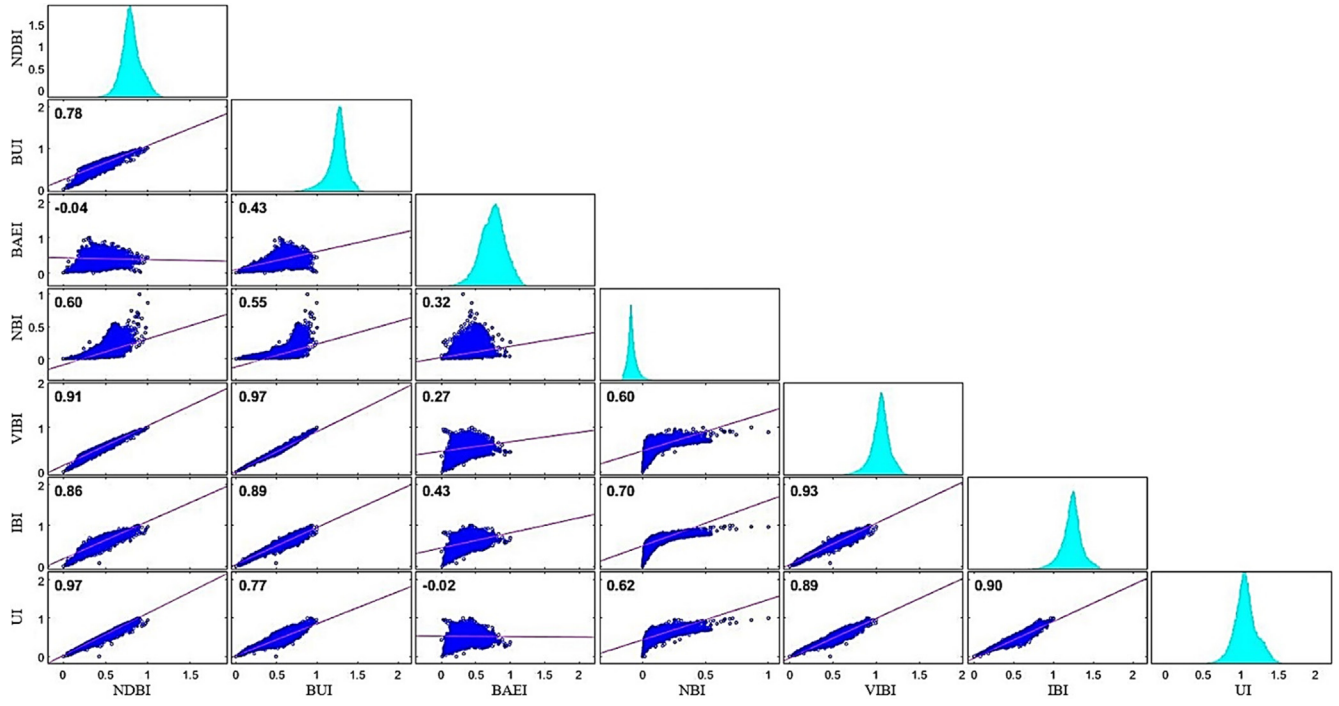

Fig. 5. Correlation between the built-up indices.

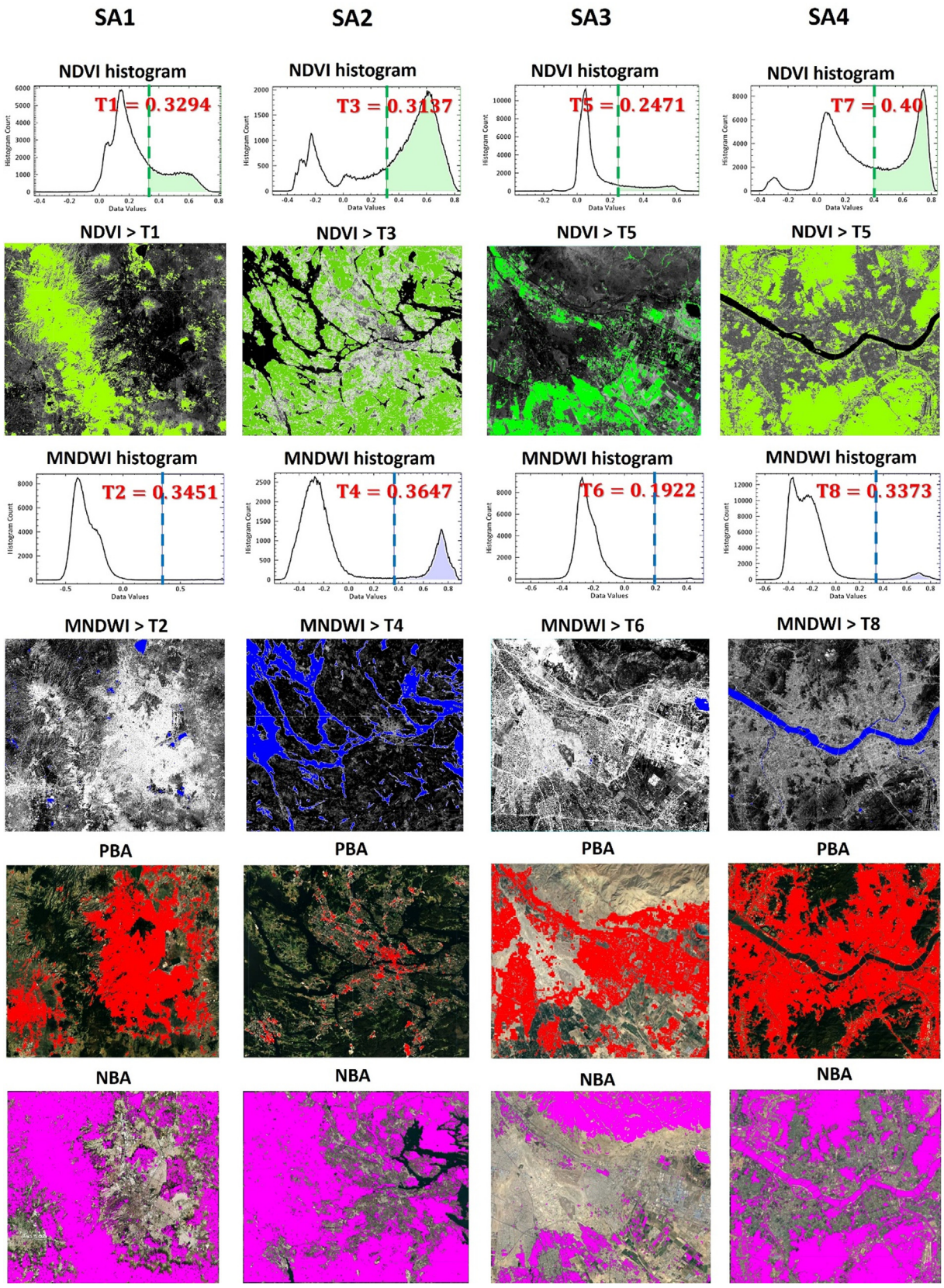

Fig. 6. The results of Otsu thresholding and the obtained PBAs and NBAs.

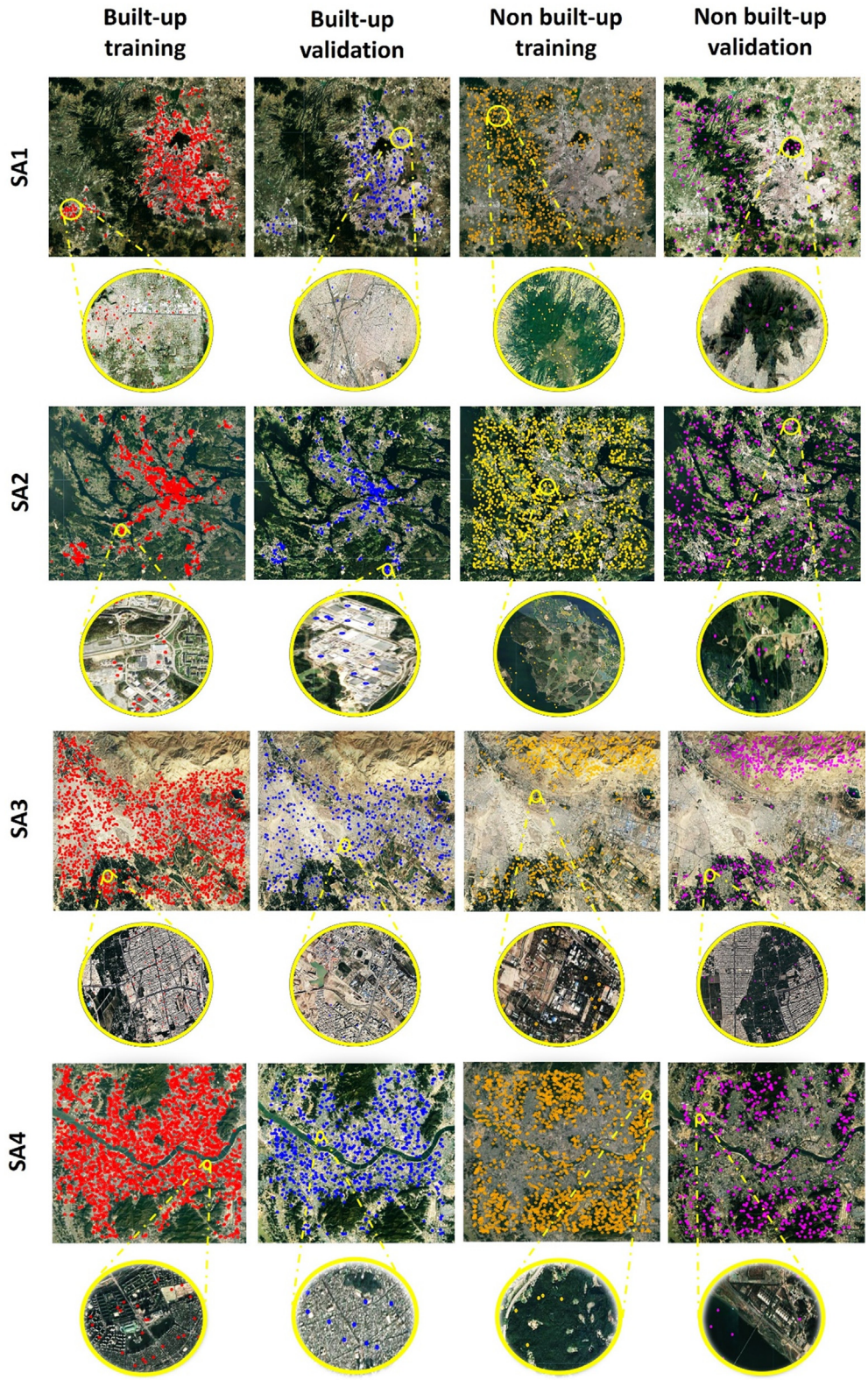

Fig. 7. Training and validation sample collections.

outputs are acceptable (Chen et al., 2018c). The obtained results of our proposed method were also visually compared with some other state-of-the-art national and global built-up maps (Fig. 10). The products include 1000 m-Global Human Settlement Layers (GHSL) (Pesaresi et al., 2016), 100 m-Copernicus Global Land Cover Layers, i.e., CGLS-LC100 Collection 3 (CGLS) (Buchhorn et al., 2020), ESA WorldCover 10 m v100 (ESA WC) (Van De

Table 4
Number of training and validation samples*.

SA	Class	Training (Pts)	Validation (Pts)	Total (Pts)
Mexico City	BA	769	231	1,000
	NBA	1,044	256	1,300
Total (Pts)		1,813	487	
Stockholm	BA	1612	388	2,000
	NBA	1579	421	2,000
Total (Pts)		3,191	809	
Tehran	BA	778	222	1,000
	NBA	757	243	1,000
Total (Pts)		1,535	465	
Seoul	BA	2,326	674	3,000
	NBA	1,565	435	2,000
Total (Pts)		3,891	1,109	

* BA: built-up; NBA: non-built-up; Pts: points; and SA: study area.

Kerchove et al., 2021; EEDC, 2022a), 10 m-World settlement footprint 2015 (WSF 2015) (Marconcini et al., 2020), Dynamic World (DW) V1 (Brown et al., 2022), MODIS MCD12Q1 V6 (Friedl and Sulla-Menashe, 2019), Copernicus CORINE Land Cover (CLC) (CLC2018, 2020), and 10 m-Iran Land Cover Map (ILCM) (Ghorbanian et al., 2020).

The results showed that all the methods similarly and effectively extracted the general pattern of urban built-up areas and that the slight differences are related to some challenging areas such as bare lands (which are similar to built-up areas from the visual/spectral similarity point of view) and narrow road network. By scrutinizing the results and comparing them with each other, it is found that our proposed method effectively extracts built-up areas and

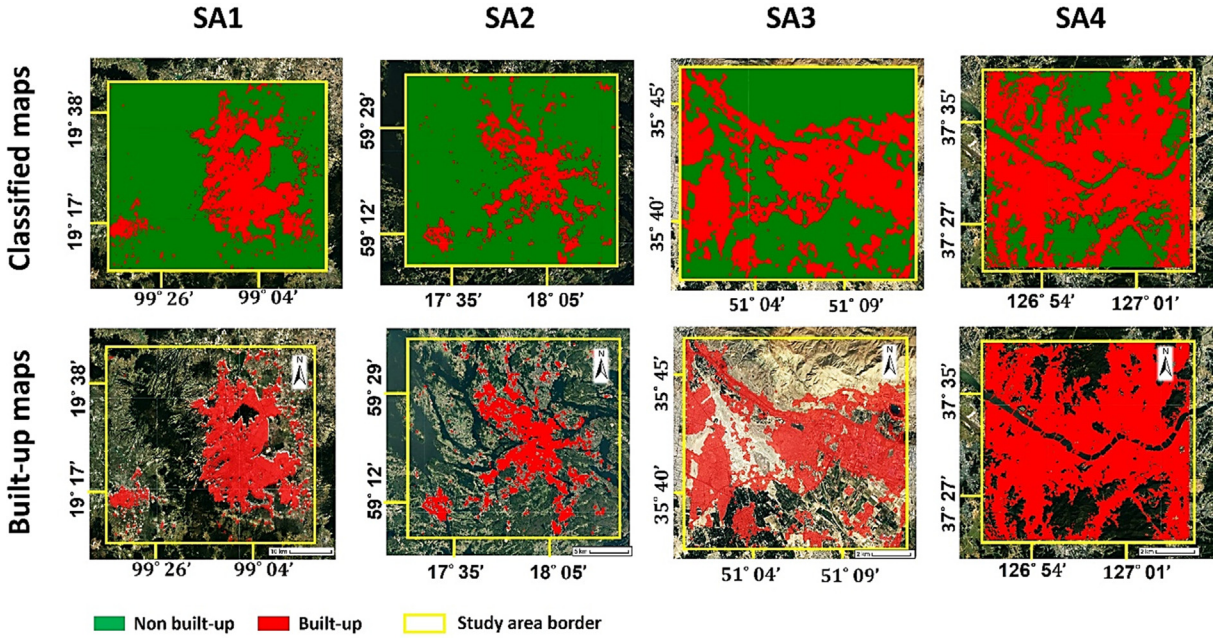

Fig. 8. The RCM_F and final built-up maps produced by our method.

Confusion matrices

classes		references BU	references NBU	CE	UA (%)
classification	BU	228	8	0.03	0.98
	NBU	3	253	0.01	0.96
OE		0.01	0.03	OA = 97.7	
PA (%)		0.96	0.98	K = 0.954	

(a)

classes		references BU	references NBU	CE	UA (%)
classification	BU	436	3	0.006	0.93
	NBU	30	418	0.07	0.99
OE		0.06	0.007	OA = 96.2	
PA (%)		0.99	0.93	K = 0.925	

(b)

classes		references BU	references NBU	CE	UA (%)
classification	BU	201	20	0.09	0.99
	NBU	1	241	0.004	0.92
OE		0.004	0.08	OA = 95.5	
PA (%)		0.90	0.99	K = 0.908	

(c)

classes		references BU	references NBU	CE	UA (%)
classification	BU	654	18	0.02	0.85
	NBU	114	318	0.35	0.95
OE		0.17	0.05	OA = 88.1	
PA (%)		0.97	0.74	K = 0.738	

(d)

Fig. 9. Confusion matrices of our method in different study areas: (a) SA1; (b) SA2; (c) SA3; and (d) SA4.

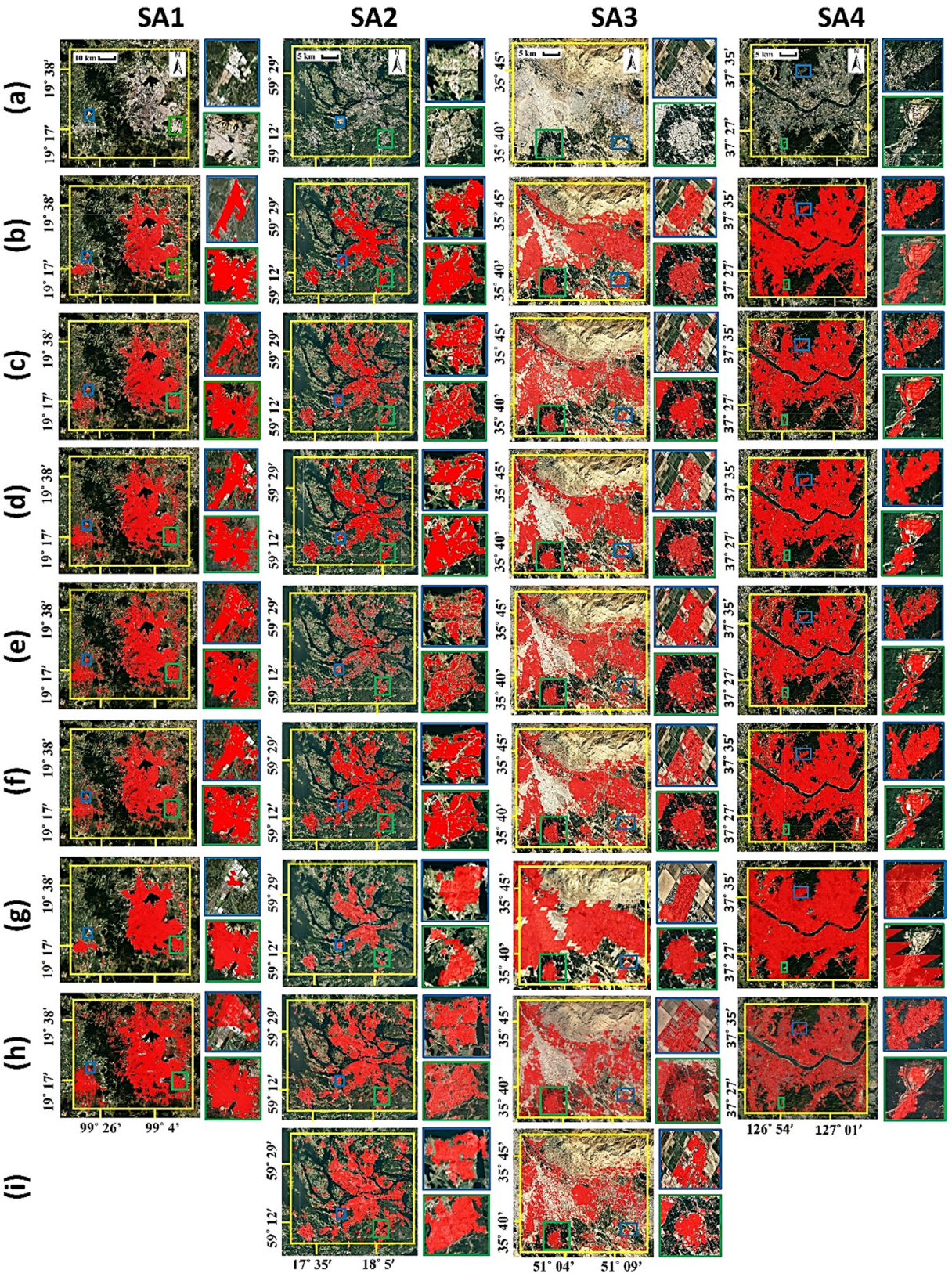

Fig. 10. Visual comparison between our method and other state-of-the-art methods: (a) Google Earth images; (b) Our method; (c) GHSL; (d) CGLS; (e) ESA WC; (f) WSF; (g) MCD12Q1; (h) DW V1; and (i) Local built-up maps (CLC and ILCM for SA2 and SA3, respectively).

that even it has a good ability to map narrow roads. Furthermore, the GHSL and ESA WC, with a spatial resolution of 30 m and 10 m, respectively, are two of the other powerful methods that can effectively extract urban road networks. Among the four high-resolution (10 m) built-up maps, i.e. our produced maps, CLC, and DW V1, and WSF, the first two better match the Google Earth ground truth, while in DW V1 and WSF there are some slight discontinuities which are less consistent with reality. Due to its spatial resolution (100 m) and with an OA of about 80% (which was declared in Buchhorn et al., 2020), the CGLS product can extract the overall pattern of urban built-up areas, and it can model the road structure with a width less than 100 m. Furthermore, with a resolution of about 500 m, MCD12Q1 is not able to extract small built-up areas, i.e. like CGLS only mapped the urban area in a relatively coarse scale. Our results and the WSF product have the most similarity in terms of visual characteristics, i.e. in both of them, there are the least possible discontinuities in the final map. The two-level post-classification in our method provides us with such results with the least unreal discontinuities. For the SA3, the result of our method is compared to 10 m-ILCM. According to Ghorbanian et al. (2020), ILCM was produced with an OA of 95.6%, which shows that our method had good accuracy in the extraction of built-up areas in SA3 (Note that our method has an OA of about 95.5% in SA3). It can be seen that the OA and Kappa in SA4′s results are smaller than other SAs. To investigate the reason for this, it can be argued that due to the nature of our proposed method, the algorithm has been run several times and different amounts of training and validation samples have been set each time. The experiments indicate no significant variation of OA and Kappa in this case. Moreover, based on Liu et al.'s (2019) research, it was revealed that with a constant number of training and validation samples, different built-up extraction methods such as FROM-GLC, PII, and GUL can have considerably different performances in different case studies. Therefore, it is quite possible for a single method to perform completely different in various cases. In addition, finding out the exact reason for this still requires more effort.

In order to analyze the impact of the classifier algorithm in the classification process, the statistical difference of the SVM result is compared to that of the other well-known classifier, i.e. Random Forest (RF). For such a comparison, the non-parametric McNemar's statistical test is used, which defines a standardized normal indicator as Eq. (31) (McNemar, 1947; Samadzadegan et al., 2017).

$$Z = \frac{f_{12} - f_{21}}{\sqrt{f_{12} + f_{21}}} \tag{31}$$

where f_{12} indicates the number of samples classified correctly by SVM and incorrectly by RF, and f_{21} indicates the number of samples classified correctly by RF and incorrectly by SVM.

The test is carried out on the Seoul case study (SA4) in which more samples (compared to the other three study areas) are involved in its classification process. For the same training and validation samples (similar to that was used for SVM), the confusion matrix was obtained as Eq. (32) and Eq. (33) for SVM and RF, respectively. Thus $Z = 1.63$ indicates that the difference in accuracy between the two classifiers is not statistically significant (as |Z|less than1.96). Furthermore, as Z greater than 0, it is inferred that SVM is relatively more accurate than RF (Samadzadegan et al., 2017). The indicator revealed that our results are not much dependent on the classifier method and that any well-established classifier with such a large number of training samples and rich datasets can provide acceptable results.

$$E_{SVM} = \begin{bmatrix} \mathrm{BU}_{\mathrm{reference}} : 654 & \mathrm{NBU}_{\mathrm{reference}} : 18 \\ \mathrm{BU}_{\mathrm{classification}} : 114 & \mathrm{NBU}_{\mathrm{classification}} : 318 \end{bmatrix} \tag{32}$$

$$E_{RF} = \begin{bmatrix} \mathrm{BU}_{\mathrm{reference}} : 655 & \mathrm{NBU}_{\mathrm{reference}} : 17 \\ \mathrm{BU}_{\mathrm{classification}} : 119 & \mathrm{NBU}_{\mathrm{classification}} : 313 \end{bmatrix} \tag{33}$$

One of the most prominent strength points of our real-time method, compared to its competitors, is its high flexibility. By the term "flexibility," we mean that one can easily manipulate the hybrid feature set (increase or decrease the layers), the size of sample collections, and the key parameters as fast as possible and re-run the algorithm for the same (or even other) case study without running into any trouble. Furthermore, the joint automatic and manual modules for sample selection led to producing a sample feature collection from all kinds of built-up characteristics. This provides a diverse and rich set of training data for training the SVM classifier and prevents overfitting in the classification of new inputs (as the classifier is trained with a variety of diverse samples from all over the study area and it is somehow saturated). In order to guarantee the robustness of our method against the study area, i.e. to investigate if its performance depends on the study area and also to find out whether or not it works for any area with different built-up characteristics, it should be implemented for a large number of study areas (e.g. for tens of cases) all over the world.

Our proposed method was implemented on a laptop with a 2.50 GHz Pentium Intel Core i7 CPU, NVIDIA GeForce MX 130 GPU, and 16 GB of RAM. However, Internet speed is very more important than hardware characteristics. With a 10 Mb/s Internet speed, GEE codes consume about three minutes to be run for the study areas of this paper. As a result, the performance on national and global scales would be time-consuming while having about 1,000–3,000 samples and a hybrid feature set containing more than 15 STS bands. In the case of online cloud-computing server-client platforms, such as GEE, where a great portion of computational affairs are conducted on the server side and only the final desired results are sent to the client side, the process gets accelerated considerably, compared to the traditional offline desktop-based image processing platforms.

As the LJ 1–01 satellite was launched very recently (in June 2018), its images do not cover the whole globe

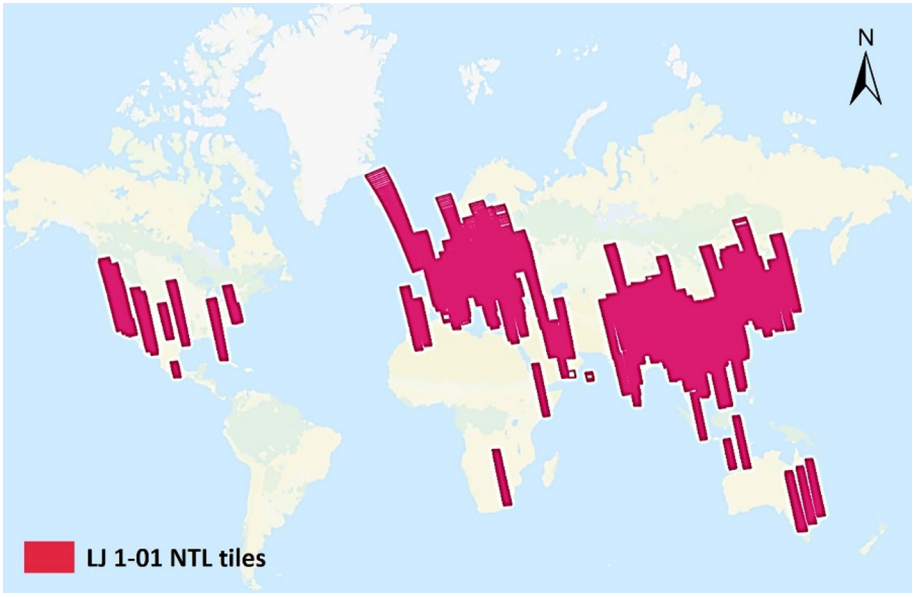

Fig. 11. The global coverage of the LJ 1–01 NTL data (source: Hubei data and application network).

(Fig. 11 shows that by the year 2022, about 30% of the world is covered by 8,673 NTL image frames), and also they have not been provided by the GEE platform yet. In the upcoming years, by having the LJ 1–01 images in the GEE data repository, it can be a good opportunity to automatically extract the built-up areas for the whole globe with a spatial resolution of 10 m and also to monitor dynamic changes of built-up areas within two epochs in real-time mode.

5. Conclusions

In this study, we proposed a fully automatic method to integrate the LJ 1–01 NTL data, Sentinel-1 SAR, and Sentinel-2 multispectral imagery for real-time mapping of urban built-up areas in the GEE platform. A hybrid STS feature space was established and was accompanied by the training and validation sample collections, and then they were entered into the well-established SVM classification. The samples were automatically collected based on the LJ image and the water and vegetation masks generated by the Sentinel-2 imagery and applying thresholding. The hybrid STS feature set was classified to produce a preliminary built-up map. Then, the mentioned map was automatically improved in the two-level post-classification process. The proposed method with an average OA of 94.4% was shown to efficiently extract the built-up area. Also, compared to other state-of-the-art methods, our algorithm has promising performance.

One of the good characteristics of our method is using the cloud computing GEE platform, and this makes it suitable to be implemented in other case studies all over the globe. In this study, GEE was shown to have a brilliant capability to process multi-gigabyte big satellite data and produce desired built-up maps in a short time. Our method may face some challenges. For instance, although we filtered the input images to have the least possible cloud-free data, the cloud may cause some problem for the results by affecting the Sentinel-2 image, and the challenge may intensify when the study area drastically increases (e.g., for the whole globe). Furthermore, obviously due to the limitations in the input data, our method is not able to map the urban roads with a width lower than the spatial resolution of the Sentinel-2 images (10 m).

For future research to improve the performance of our method, one can implement the algorithm using the DL-based method (instead of traditional ML-based methods such as SVM, RF, etc.) by linking the GEE and Google Colaboratory (Colab) platforms. In order to make other improvements in future research, one can use the super-resolution (SR)-based DL techniques to sharpen the initial Sentinel MS bands using their own spatial information (Zhong et al., 2016) or the high-resolution SkySat and NAIP satellite and aerial images provided by GEE[2] (EEDC, 2022b). The image sharpening led to producing enhanced Sentinel data with a spatial resolution better than 10 m. It is worth noting that in Zhong et al.'s (2016) self-enhancement technique the resolution of the Sentinel images improves using the spatial information of the Sentinel multispectral bands themselves. Furthermore, a distinct module can be set up for extraction of road networks out of the LJ 1–01 NTL data by distinguishing the urban regions through a threshold-based method and by means of an unsupervised pulse coupled neural network (PCNN) (Wang et al., 2021). The output of the road extraction module can be aggregated with our base built-

[2] These images are provided only for some parts of the Earth and also for some limited dates.

up mapping method using an AND logical operation to obtain the final built-up areas.

We hope that this research will open new horizons to the RS scientific community and that its promising results will be useful for them. Furthermore, it is desired that, according to these geospatial maps, the decision makers make appropriate and effective decisions toward sustainable development.

Declaration of Competing Interest

The authors declare that they have no known competing financial interests or personal relationships that could have appeared to influence the work reported in this paper.

References

Al-Wassai, F. A., Kalyankar, D. N., 2012. A novel metric approach evaluation for the spatial enhancement of pan-sharpened images. *arXiv preprint arXiv:1207.5064*.

Ban, Y., Jacob, A., Gamba, P., 2015. Spaceborne SAR data for global urban mapping at 30 m resolution using a robust urban extractor. ISPRS J. Photogramm. Remote Sens. 103, 28–37.

Bhatti, S.S., Tripathi, N.K., 2014. Built-up area extraction using Landsat 8 OLI imagery. GIScience & Remote Sens. 51 (4), 445–467.

Bioresita, F., Puissant, A., Stumpf, A., Malet, J.P., 2018. A method for automatic and rapid mapping of water surfaces from sentinel-1 imagery. Remote Sens. (Basel) 10 (2), 217.

Bouzekri, S., Lasbet, A.A., Lachehab, A., 2015. A new spectral index for extraction of built-up area using Landsat-8 data. J. Indian Soc. Remote Sens. 43 (4), 867–873.

Brown, C.F., Brumby, S.P., Guzder-Williams, B., Birch, T., Hyde, S.B., Mazzariello, J., Tait, A.M., 2022. Dynamic World, Near real-time global 10 m land use land cover mapping. Sci. Data 9 (1), 251.

Buchhorn, M., Lesiv, M., Tsendbazar, N.E., Herold, M., Bertels, L., Smets, B., 2020. Copernicus global land cover layers—collection 2. Remote Sens. (Basel) 12 (6), 1044.

Cao, X., Chen, J., Imura, H., Higashi, O., 2009. A SVM-based method to extract urban areas from DMSP-OLS and SPOT VGT data. Remote Sens. Environ. 113 (10), 2205–2209.

Chen, Y., Ge, Y., An, R., Chen, Y., 2018a. Super-resolution mapping of impervious surfaces from remotely sensed imagery with points-of-interest. Remote Sens. (Basel) 10 (2), 242.

Chen, Y., Lv, Z., Huang, B., Jia, Y., 2018b. Delineation of built-up areas from very high-resolution satellite imagery using multi-scale textures and spatial dependence. Remote Sens. (Basel) 10 (10), 1596.

Chen, Y., Lu, D., Moran, E., Batistella, M., Dutra, L.V., Sanches, I.D.A., da Silva, R.F.B., Huang, J., Luiz, A.J.B., de Oliveira, M.A.F., 2018c. Mapping croplands, cropping patterns, and crop types using MODIS time-series data. Int. J. Appl. Earth Obs. Geoinf. 69, 133–147.

Chen, X., Zhang, F., Du, Z., Liu, R., 2020. An Unsupervised Urban Extent Extraction Method from NPP-VIIRS Nighttime Light Data. Remote Sens. (Basel) 12 (22), 3810.

CLC 2018, 2020. In: Copernicus. https://land.copernicus.eu/pan-european/corine-land-cover/clc2018?tab=metadata. Accessed 29 Jan 2023.

Darmanto, N.S., Varquez, A.C.G., Kanda, M., 2015. Detection of Urban Environment from Landsat 8 for Mesoscale Modeling Purposes. In: Proceeding of the 9th International Conference on Urban Climate.

Dell'Acqua, F., Gamba, P., 2006. Discriminating urban environments using multiscale texture and multiple SAR images. Int. J. Remote Sens. 27 (18), 3797–3812.

Djerriri, K., Benyelles, Z., Attaf, D., Cheriguene, R.S., October.. Extraction of built-up areas from remote sensing imagery using one-class classification. Image and Signal Processing for Remote Sensing XXV, 11155. SPIE, pp. 610–616.

Dou, Y., Liu, Z., He, C., Yue, H., 2017. Urban land extraction using VIIRS nighttime light data: an evaluation of three popular methods. Remote Sens. (Basel) 9 (2), 175.

Earth Engine Data Catalogue (EEDC), 2022a. https://developers.google.com/earthengine/datasets/catalog/ESA_WorldCover_v100.

EEDC, 2022b. https://developers.google.com/earth-engine/datasets/catalog/SKYSAT_GEN-A_PUBLIC_ORTHO_MULTISPECTRAL.

Esch, T., Heldens, W., Hirner, A., Keil, M., Marconcini, M., Roth, A., Zeidler, J., Dech, S., Strano, E., 2017. Breaking new ground in mapping human settlements from space–The Global Urban Footprint. ISPRS J. Photogramm. Remote Sens. 134, 30–42.

Ettehadi Osgouei, P., Kaya, S., Sertel, E., Alganci, U., 2019. Separating built-up areas from bare land in mediterranean cities using Sentinel-2A imagery. Remote Sens. (Basel) 11 (3), 345.

Farhadi, H., Managhebi, T., Ebadi, H., 2022. Buildings extraction in urban areas based on the radar and optical time series data using Google Earth Engine. Scientific-Research Quart. Geogr. Data (SEPEHR) 30 (120), 43–63.

Friedl, M., Sulla-Menashe, D., 2019. *MCD12Q1 MODIS/Terra+Aqua Land Cover Type Yearly L3 Global 500m SIN Grid V006* . NASA EOSDIS Land Processes DAAC. Accessed 2023-01-29 from https://doi.org/10.5067/MODIS/MCD12Q1.006.

Ghorbanian, A., Kakooei, M., Amani, M., Mahdavi, S., Mohammadzadeh, A., Hasanlou, M., 2020. Improved land cover map of Iran using Sentinel imagery within Google Earth Engine and a novel automatic workflow for land cover classification using migrated training samples. ISPRS J. Photogramm. Remote Sens. 167, 276–288.

Ghosh, D.K., Mandal, A.C., Majumder, R., Patra, P., Bhunia, G.S., 2018. Analysis for mapping of built-up area using remotely sensed indices–a case study of Rajarhat Block in Barasat Sadar Sub-Division in West Bengal (India). J. Landscape Ecol. 11 (2), 67–76.

GIS, 2011. https://gis.stackexchange.com/questions/6412/generating-points-that-lie-inside-polygon-using-qgis.

Gong, P., Wang, J., Yu, L., Zhao, Y., Zhao, Y., Liang, L., Chen, J., 2013. Finer resolution observation and monitoring of global land cover: First mapping results with Landsat TM and ETM+ data. Int. J. Remote Sens. 34 (7), 2607–2654.

Guo, W., Zhang, Y., Gao, L., 2018. Using VIIRS-DNB and landsat data for impervious surface area mapping in an arid/semiarid region. Remote sensing letters 9 (6), 587–596.

Haralick, R.M., Shanmugam, K., Dinstein, I.H., 1973. Textural features for image classification. IEEE Trans. Syst. Man Cybern. 6, 610–621.

He, C., Shi, P., Xie, D., Zhao, Y., 2010. Improving the normalized difference built-up index to map urban built-up areas using a semiautomatic segmentation approach. Remote Sens. Lett. 1 (4), 213–221.

He, C., Liu, Z., Tian, J., Ma, Q., 2014. Urban expansion dynamics and natural habitat loss in China: A multiscale landscape perspective. Glob. Chang. Biol. 20 (9), 2886–2902.

He, C., Liu, Z., Gou, S., Zhang, Q., Zhang, J., Xu, L., 2019. Detecting global urban expansion over the last three decades using a fully convolutional network. Environ. Res. Lett. 14 (3) 034008.

He, X., Zhang, Z., Yang, Z., 2021. Extraction of urban built-up area based on the fusion of night-time light data and point of interest data. R. Soc. Open Sci. 8 (8) 210838.

Hidayati, I. N., Suharyadi, R., Danoedoro, P., 2018, April. Developing an extraction method of urban built-up area based on remote sensing imagery transformation index. In: Forum Geografi (Vol. 32, No. 1, pp. 96-108).

Holobâcă, I.H., Ivan, K., Alexe, M., 2019. Extracting built-up areas from Sentinel-1 imagery using land-cover classification and texture analysis. Int. J. Remote Sens. 40 (20), 8054–8069.

Hu, Y.N., Peng, J., Liu, Y., Du, Y., Li, H., Wu, J., 2017. Mapping development pattern in Beijing-Tianjin-Hebei urban agglomeration using DMSP/OLS nighttime light data. Remote Sens. (Basel) 9 (7), 760.

Huang, B., Zhao, B., Song, Y., 2018. Urban land-use mapping using a deep convolutional neural network with high spatial resolution

multispectral remote sensing imagery. Remote Sens. Environ. 214, 73–86.
Huete, A.R., 1988. A soil-adjusted vegetation index (SAVI). Remote Sens. Environ. 25 (3), 295–309.
Iannelli, G.C., Lisini, G., Dell'Acqua, F., Feitosa, R.Q., Costa, G.A.O.P. D., Gamba, P., 2014. Urban area extent extraction in spaceborne HR and VHR data using multi-resolution features. Sensors 14 (10), 18337–18352.
Iino, S., Ito, R., Doi, K., Imaizumi, T., Hikosaka, S., 2018. CNN-based generation of high-accuracy urban distribution maps utilising SAR satellite imagery for short-term change monitoring. Int. J. Image Data Fusion 9 (4), 302–318.
Jafari, S., Attarchi, S., 2021. Detection of urban built-up areas by using Sentinel-1images from different orbits, Case study: Isfahan. Geographical Urban Planning Research (GUPR) 9 (3), 709–734.
Javan, F.D., Samadzadegan, F., Mehravar, S., Toosi, A., 2019. A review on spatial quality assessment methods for evaluation of pan-sharpened satellite imagery. Int. Arch. Photogramm. Remote Sens. Spat. Inf. Sci 42, 255–261.
Jia, Y., Ge, Y., Chen, Y., Li, S., Heuvelink, G.B., Ling, F., 2019. Super-resolution land cover mapping based on the convolutional neural network. Remote Sens. (Basel) 11 (15), 1815.
Jieli, C., Manchun, L.I., Yongxue, L.I.U., Chenglei, S. and Wei, H.U., 2010, June. Extract residential areas automatically by new built-up index. In: 2010 18th International Conference on Geoinformatics. IEEE, pp. 1-5.
Karaca, Y., Cattani, C., Moonis, M., July.. Comparison of deep learning and support vector machine learning for subgroups of multiple sclerosis. In: International Conference on Computational Science and Its Applications. Springer, Cham, pp. 142–153.
Kawamura, M., 1996. Relation between social and environmental conditions in Colombo Sri Lanka and the urban index estimated by satellite remote sensing data. In: Proc. 51st Annual Conference of the Japan Society of Civil Engineers, pp. 190-191.
Lai, Y., October.. A comparison of traditional machine learning and deep learning in image recognition. Journal of Physics: Conference Series Vol. 1314, No. 1.
Lefebvre, A., Sannier, C., Corpetti, T., 2016. Monitoring urban areas with Sentinel-2A data: Application to the update of the Copernicus high resolution layer imperviousness degree. Remote Sens. (Basel) 8 (7), 606.
Li, S., Fu, S., Zheng, D., 2022. Rural built-up area extraction from remote sensing images using spectral residual methods with embedded deep neural network. Sustainability 14 (3), 1272.
Li, Y., Tan, Y., Deng, J., Wen, Q., Tian, J., 2015. Cauchy graph embedding optimization for built-up areas detection from high-resolution remote sensing images. IEEE J. Sel. Top. Appl. Earth Obs. Remote Sens. 8 (5), 2078–2096.
Li, J., Zhang, R., Li, Y., 2016. Multiscale convolutional neural network for the detection of built-up areas in high-resolution SAR images. In: 2016 IEEE International Geoscience and Remote Sensing Symposium (IGARSS). IEEE, pp. 910–913.
Li, X., Zhao, L., Li, D., Xu, H., 2018. Mapping urban extent using Luojia 1–01 nighttime light imagery. Sensors 18 (11), 3665.
Li, X., Zhou, Y., 2017. Urban mapping using DMSP/OLS stable night-time light: a review. Int. J. Remote Sens. 38 (21), 6030–6046.
Li, X., Liu, Z., Chen, X., Sun, J., 2019. Assessing the ability of Luojia 1–01 imagery to detect feeble nighttime lights. Sensors 19 (17), 3708.
Liu, C., Yang, K., Bennett, M.M., Guo, Z., Cheng, L., Li, M., 2019. Automated extraction of built-up areas by fusing VIIRS nighttime lights and Landsat-8 data. Remote Sens. (Basel) 11 (13), 1571.
Lu, D., Tian, H., Zhou, G., Ge, H., 2008. Regional mapping of human settlements in southeastern China with multisensor remotely sensed data. Remote Sens. Environ. 112 (9), 3668–3679.
Marconcini, M., Metz-Marconcini, A., Üreyen, S., Palacios-Lopez, D., Hanke, W., Bachofer, F., Zeidler, J., Esch, T., Gorelick, N., Kakarla, A., Paganini, M., 2020. Outlining where humans live, the World Settlement Footprint 2015. Sci. Data 7 (1), 1–14.
McFeeters, S.K., 1996. The use of the Normalized Difference Water Index (NDWI) in the delineation of open water features. Int. J. Remote Sens. 17 (7), 1425–1432.
Mhangara, P., Mapurisa, W., Mudau, N., 2020. Image interpretability of nSight-1 nanosatellite imagery for remote sensing applications. Aerospace 7 (2), 19.
Mohammadnejad, V., 2020. Urban lands Extraction from Sentinel 1 and 2 satellite imagery based on Google Earth Engine (GEE). Geographical Urban Planning Research (GUPR) 8 (3), 613–630.
Osada, R., Funkhouser, T., Chazelle, B., Dobkin, D., 2002. Shape distributions. ACM Transactions on Graphics (TOG) 21 (4), 807–832.
Pearson, K., Blakeman, J., 1904. Mathematical contributions to the theory of evolution. XIII. On the theory of contingency and its relation to association and normal correlation.
Pesaresi, M., Freire, S., 2016: GHS Settlement grid following the REGIO model 2014 in application to GHSL Landsat and CIESIN GPW v4-multitemporal (1975-1990-2000-2015). In: European Commission, Joint Research Centre (JRC) [Dataset] PID: https://data.europa.eu/89h/jrc-ghsl ghs_smod_pop_globe_r2016a.
Prasomsup, W., Piyatadsananon, P., Aunphoklang, W., Boonrang, A., 2020. Extraction technic for built-up area classification in Landsat 8 imagery. Int. J. Environ. Sci. Dev. 11 (1), 15–20.
Rasul, A., Balzter, H., Ibrahim, G.R.F., Hameed, H.M., Wheeler, J., Adamu, B., Najmaddin, P.M., 2018. Applying built-up and bare-soil indices from Landsat 8 to cities in dry climates. Land 7 (3), 81.
GEE Reference, 2022. https://developers.google.com/earth-engine/api-docs/ee-featurecollection-randompoints.
Risky, Y.S., Aulia, Y.H. and Widayani, P., 2017, December. Spatiotemporal Built-up Land Density Mapping Using Various Spectral Indices in Landsat-7 ETM+ and Landsat-8 OLI/TIRS (Case Study: Surakarta City). In IOP Conference Series: Earth and Environmental Science (Vol. 98, No. 1). IOP Publishing, p. 012006.
Samadzadegan, F., Hasani, H., Reinartz, P., 2017. Toward optimum fusion of thermal hyperspectral and visible images in classification of urban area. Photogramm. Eng. Remote Sens. 83 (4), 269–280.
Semenzato, A., Pappalardo, S.E., Codato, D., Trivelloni, U., De Zorzi, S., Ferrari, S., De Marchi, M., Massironi, M., 2020. Mapping and monitoring urban environment through sentinel-1 SAR data: A case study in the Veneto region (Italy). ISPRS Int. J. Geo Inf. 9 (6), 375.
Sezgin, M., Sankur, B., 2004. Survey over image thresholding techniques and quantitative performance evaluation. J. Electron. Imaging 13 (1), 146–165.
Sharma, R.C., Tateishi, R., Hara, K., Gharechelou, S., Iizuka, K., 2016. Global mapping of urban built-up areas of year 2014 by combining MODIS multispectral data with VIIRS nighttime light data. Int. J. Digital Earth 9 (10), 1004–1020.
Small, C., Pozzi, F., Elvidge, C.D., 2005. Spatial analysis of global urban extent from DMSP-OLS night lights. Remote Sens. Environ. 96 (3–4), 277–291.
Small, C., Elvidge, C.D., Baugh, K., 2013. April. Mapping urban structure and spatial connectivity with VIIRS and OLS night light imagery. In: Joint Urban Remote Sensing Event 2013. IEEE, pp. 230–233.
Stackoverflow (SOF), 2011. https://stackoverflow.com/questions/4778147/sample-random-point-in-triangle.
Stathakis, D., Perakis, K., Savin, I., 2012. Efficient segmentation of urban areas by the VIBI. Int. J. Remote Sens. 33 (20), 6361–6377.
Tan, Y., Xiong, S., Yan, P., 2021. Accurate Detection of Built-Up Areas in Remote Sensing Image via Deep Learning.
Tan, Y., Xiong, S., Li, Y., 2018. Automatic extraction of built-up areas from panchromatic and multispectral remote sensing images using double-stream deep convolutional neural networks. IEEE J. Sel. Top. Appl. Earth Obs. Remote Sens. 11 (11), 3988–4004.
Tan, Y., Xiong, S., Yan, P., 2020. Multi-branch convolutional neural network for built-up area extraction from remote sensing image. Neurocomputing 396, 358–374.
Tao, C., Tan, Y., Zou, Z.R., Tian, J., 2013. Unsupervised detection of built-up areas from multiple high-resolution remote sensing images. IEEE Geosci. Remote Sens. Lett. 10 (6), 1300–1304.

Tian, T., Li, C., Xu, J., Ma, J., 2018. Urban area detection in very high resolution remote sensing images using deep convolutional neural networks. Sensors 18 (3), 904.

Toosi, A., Javan, F.D., Samadzadegan, F., Mehravar, S., Kurban, A., Azadi, H., 2022. Citrus orchard mapping in juybar, iran: Analysis of ndvi time series and feature fusion of multi-source satellite imageries. Eco. Inform. 70 101733.

Van De Kerchove, R., Zanaga, D., Keersmaecker, W., Souverijns, N., Wevers, J., Brockmann, C., Grosu, A., Paccini, A., Cartus, O., Santoro, M. and Lesiv, M., 2021, December. ESA WorldCover: Global land cover mapping at 10 m resolution for 2020 based on Sentinel-1 and 2 data. In: AGU Fall Meeting Abstracts (Vol. 2021), pp. GC45I-0915.

Wang, J., Hadjikakou, M. and Bryan, B., 2020. Mapping built-up land with high accuracy using Fourier transformation and temporal correction.

Wang, R., Wan, B., Guo, Q., Hu, M., Zhou, S., 2017. Mapping regional urban extent using NPP-VIIRS DNB and MODIS NDVI data. Remote Sens. (Basel) 9 (8), 862.

Wang, P., Zhang, G., Leung, H., 2018. Improving super-resolution flood inundation mapping for multispectral remote sensing image by supplying more spectral information. IEEE Geosci. Remote Sens. Lett. 16 (5), 771–775.

Wang, P., Wang, L., Leung, H., Zhang, G., 2020b. Super-resolution mapping based on spatial–spectral correlation for spectral imagery. IEEE Trans. Geosci. Remote Sens. 59 (3), 2256–2268.

Wang, L., Zhang, H., Xu, H., Zhu, A., Fan, H., Wang, Y., 2021. Extraction of City Roads Using Luojia 1–01 Nighttime Light Data. Appl. Sci. 11 (21), 10113.

Weizman, L., Goldberger, J., 2009. Urban-area segmentation using visual words. IEEE Geosci. Remote Sens. Lett. 6 (3), 388–392.

Xie, Y., Weng, Q., Weng, A., 2014, June. A comparative study of NPP-VIIRS and DMSP-OLS nighttime light imagery for derivation of urban demographic metrics. In: 2014 Third International Workshop on Earth Observation and Remote Sensing Applications (EORSA). IEEE, pp. 335-339.

Xie, Y., Weng, Q., 2016. Updating urban extents with nighttime light imagery by using an object-based thresholding method. Remote Sens. Environ. 187, 1–13.

Xu, H., 2008. A new index for delineating built-up land features in satellite imagery. Int. J. Remote Sens. 29 (14), 4269–4276.

Xu, T., Coco, G., Gao, J., 2020. Extraction of urban built-up areas from nighttime lights using artificial neural network. Geocarto Int. 35 (10), 1049–1066.

Xu, M., He, C., Liu, Z., Dou, Y., 2016. How did urban land expand in China between 1992 and 2015? A multi-scale landscape analysis. *PloS one* 11 (5), e0154839.

Yan, J., 2019. Extraction Urban Clusters from Geospatial Data: A Case Study from Switzerland. *arXiv preprint arXiv:1903.07270*.

Yang, W., Si, Y., Wang, D., Guo, B., 2018. Automatic recognition of arrhythmia based on principal component analysis network and linear support vector machine. Comput. Biol. Med. 101, 22–32.

Yang, C., Yu, B., Chen, Z., Song, W., Zhou, Y., Li, X., Wu, J., 2019. A spatial-socioeconomic urban development status curve from NPP-VIIRS nighttime light data. Remote Sens. (Basel) 11 (20), 2398.

Yilmaz, A., Demircali, A.A., Kocaman, S., Uvet, H., 2020. Comparison of Deep Learning and Traditional Machine Learning Techniques for Classification of Pap Smear Images. *arXiv preprint arXiv:2009.06366*.

Yu, B., Shu, S., Liu, H., Song, W., Wu, J., Wang, L., Chen, Z., 2014. Object-based spatial cluster analysis of urban landscape pattern using nighttime light satellite images: a case study of China. Int. J. Geogr. Inf. Sci. 28 (11), 2328–2355.

Yu, B., Tang, M., Wu, Q., Yang, C., Deng, S., Shi, K., Peng, C., Wu, J., Chen, Z., 2018. Urban built-up area extraction from log-transformed NPP-VIIRS nighttime light composite data. IEEE Geosci. Remote Sens. Lett. 15 (8), 1279–1283.

Yuan, X., Jia, L., Menenti, M., Zhou, J., Chen, Q., 2019. Filtering the NPP-VIIRS nighttime light data for improved detection of settlements in Africa. Remote Sens. (Basel) 11 (24), 3002.

Zha, Y., Gao, J., Ni, S., 2003. Use of normalized difference built-up index in automatically mapping urban areas from TM imagery. Int. J. Remote Sens. 24 (3), 583–594.

Zhang, T., Tang, H., 2018, November. Built-up area extraction from Landsat 8 images using convolutional neural networks with massive automatically selected samples. In: Chinese Conference on Pattern Recognition and Computer Vision (PRCV) (pp. 492-504). Springer, Cham.

Zhang, Q., Schaaf, C., Seto, K.C., 2013. The vegetation adjusted NTL urban index: A new approach to reduce saturation and increase variation in nighttime luminosity. Remote Sens. Environ. 129, 32–41.

Zhang, Q., Huang, X., Zhang, G., 2017. Urban area extraction by regional and line segment feature fusion and urban morphology analysis. Remote Sens. (Basel) 9 (7), 663.

Zhang, J., Li, P., Wang, J., 2014. Urban built-up area extraction from Landsat TM/ETM+ images using spectral information and multivariate texture. Remote Sens. (Basel) 6 (8), 7339–7359.

Zhou, S., Deng, Y., Wang, R., Li, N., Si, Q., 2017. Effective Mapping of Urban Areas Using ENVISAT ASAR, Sentinel-1A, and HJ-1-C Data. IEEE Geosci. Remote Sens. Lett. 14 (6), 891–895.

Zhou, Y., Smith, S.J., Elvidge, C.D., Zhao, K., Thomson, A., Imhoff, M., 2014. A cluster-based method to map urban area from DMSP/OLS nightlights. Remote Sens. Environ. 147, 173–185.

Zou, Y., Peng, H., Liu, G., Yang, K., Xie, Y., Weng, Q., 2017. Monitoring urban clusters expansion in the middle reaches of the Yangtze River, China, using time-series nighttime light images. Remote Sens. (Basel) 9 (10), 1007.